Andreev spectroscopy of the triplet-superconductor state in the Bi/Ni bilayer system

Xin Shang [1,2] Haiwen Liu,[1,2,*] and Ke Xia[2,3,†]

[1]*Department of Physics, Beijing Normal University, Beijing 100875, China*
[2]*The Center for Advanced Quantum Studies, Beijing Normal University, Beijing 100875, China*
[3]*Beijing Computational Science Research Center, Beijing 100193, China*

We calculate the Andreev spectroscopy between a ferromagnetic lead and a Bi/Ni bilayer system. The bilayer system is described by the Anderson-Brinkman-Morel (ABM) state and mixing ABM and *S*-wave states. In both the ABM state and ABM state is mixed with small *S*-wave state, the Andreev conductance is consistent with that obtained in the point-contact experiment [Zhao *et al.*, arXiv:1810.10403]. Moreover, the conductance peak near zero energy is induced by the surface state of the ABM state. Our work may provide helpful clarification for understanding recent experiments.

I. INTRODUCTION

Triplet *p*-wave superconductors have received much interest [1], providing insight into topological superfluidity [2,3], superconductivity, and spintronics applications [4,5]. Topological *p*-wave superconductors [6–8] especially promise quantum computing applications such as Majorana fermions which locate at the edges and the vortex cores of superconductors [9–14]. Topological *p*-wave superfluids of ^{3}He have been reported [15] and superconductivity in Sr_2RuO_4 has been suggested [16,17]. Another peculiar feature of topological materials is gapless surface states [17–20]. Experimentally, the surface state can be detected by the Andreev spectroscopy [17,21,22].

Recent point-contact experiments have observed triplet superconductivity in epitaxial Bi/Ni bilayers [23–25]. Triplet *p*-wave superconductivity was inferred from the zero-bias peak of the Andreev conductance between the epitaxial Bi/Ni bilayer and the ferromagnetic metal (FM). Furthermore, a quantitative analysis of the Andreev conductance revealed a triplet *p*-wave Anderson-Brinkman-Morel (ABM) state [26,27] with two Weyl nodes [3,28]. In contrast, a recent time-domain THz spectroscopy experiment [29] has reported a nodeless bulk superconductivity in the epitaxial Bi/Ni bilayer. In addition, the inversion symmetry of the Bi/Ni bilayer is broken, suggesting the mixing of different pairings such as *S*-wave and *p*-wave [30,31]. The Bi/Ni bilayer system naturally raises two questions: (1) Does the broken inversion symmetry admit any superconducting pairing other than the ABM state at the interface? (2) Given the importance of the behavior of surface states in topological superconductors, how do those surface states and bulk ABM states contribute to the transport properties?

We build a model that calculates the Andreev spectroscopy and local density of states (LDOS) of superconducting materials that may exist in the Bi/Ni bilayer, i.e., the ABM state and the ABM state mixture with *S*-wave pairing. We first calculate the conductance of the Andreev reflection in pure ABM states using the Blonder-Tinkham-Klapwijk (BTK) method [31,32] and its LDOS by the surface Green's function method [33–35]. Second, since there may be mixing in different superconducting states, we then calculate the Andreev conductance of one of the possible mixed forms: ABM mixed *S*-wave superconducting states. We find that the Andreev conductance of both the pure ABM state and the mixed state with a small *S*-wave component were consistent with the results of point-contact experiments [24]. However, in mixed states with a large *S*-wave component, the conductance deviated from the point-contact results [24]. After computing the LDOS of those states, we find nodes in the pure ABM state and the mixed state with small *S*-wave components, but not in the mixed state with a large *S*-wave component. The local density of states of the mixed state with a large *S*-wave component is consistent with the time-domain THz spectroscopy experiment [29]. We also revealed that the conductance peak near the zero energy is contributed by the surface state.

The remainder of this paper is organized as follows. Section II introduces our model for calculating the conductance. Sections III and IV calculate the conductances and the surface states of the ABM state and an unconventional superconductivity state (an ABM state mixed with an *S*-wave state), respectively. The paper concludes with a brief summary.

II. MODEL

Since the superconducting pairing function of the ABM state is isotropic on the x-y plane, in order to better describe the topological properties of ABM state, we consider a two-dimensional normal metal-superconductor (N-S) junction located at z = 0 (where z > 0 represents the superconductor, and z < 0 represents normal metal) as shown in Fig 1(a). In
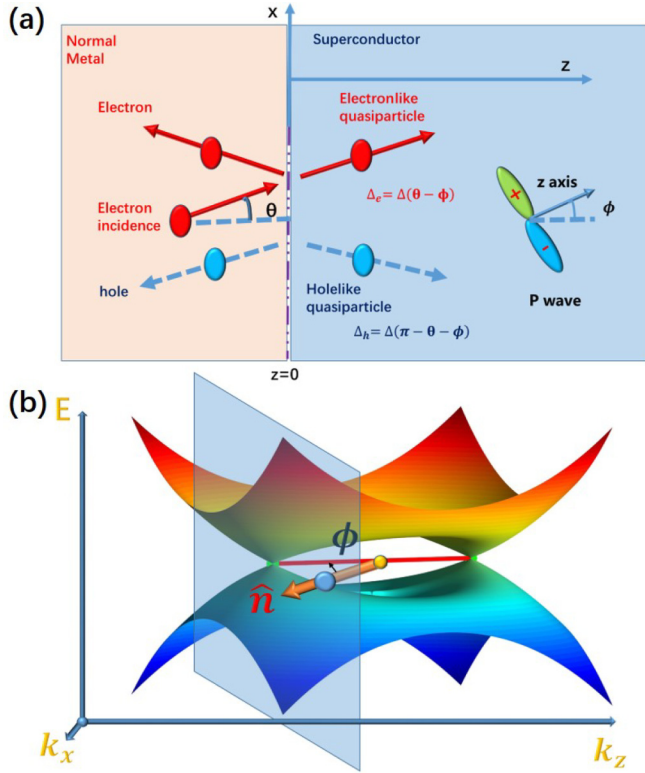
*haiwen.liu@bnu.edu.cn
†kexia@bnu.edu.cn

FIG. 1. Schematic diagram of (a) the transport system and (b) the band structure of the ABM state. ϕ represents the angle between the z axis of the p wave and the normal to the interface. The transmitted holelike and electronlike quasiparticles have effective pairing potentials of $\Delta_e = \Delta_p \sin(\theta - \phi)$ and $\Delta_h = \Delta_p \sin(\pi - \theta - \phi)$, respectively.

addition, the results of the two-dimensional tunnel junction can be extended to the three-dimensional case by integrating on the x-y plane. The effective Hamiltonian in the Nambu representation is given by [31]:

$$H_S = \begin{pmatrix} \hat{H}_0(k) & \hat{\Delta}(k) \\ -\hat{\Delta}^*(-k) & -\hat{H}_0^*(-k) \end{pmatrix}, \qquad (1)$$

where $\hat{H}_0(k) = \zeta_k$, $\zeta_k = \frac{\hbar^2}{2m}k^2 - \mu$, $\hat{\Delta}(k) = i\Delta\sigma_y$ for singlet pairing and $\hat{\Delta}(k) = [\hat{d}(k) \cdot \vec{\sigma}]i\sigma_y$ for triplet pairing [31].

We first consider the superconducting order parameter Δ_p of a p-wave superconductor in the pure ABM state [26,27]:

$$\hat{\Delta}(k) = \begin{bmatrix} -\Delta_p \sin\theta_k & 0 \\ 0 & \Delta_p \sin\theta_k \end{bmatrix}, \qquad (2)$$

where $\sin\theta_k \equiv \frac{k_{Fx}}{k_F}$ with k_F being the Fermi momentum and k_{Fx} being the x component of k_F. According to BTK theory [31,32], the wave function of a superconductor Ψ_s is given by

$$e^{ik_x x}[c_1\psi_1 e^{iq_{1z}^+ z} + c_2\psi_2 e^{-iq_{2z}^+ z} + c_3\psi_3 e^{iq_{1z}^- z} + c_4\psi_4 e^{-iq_{2z}^- z}], \qquad (3)$$

where $q_{1(2)z}^{\pm} = \sqrt{q_{1(2),\pm}^2 - k_{Fx}^2}$, $q_{1(2),\pm}^2 \approx k_F$. Here, $\psi_{1(2)} = [u_{e(h)}^+, 0, -v_{e(h)}^+, 0]^T$ denotes the electronlike (holelike) state for spin index $\uparrow$, and $\psi_{3(4)} = [0, u_{e(h)}^-, 0, v_{e(h)}^-]^T$ denotes the electronlike (holelike) state for spin index $\downarrow$, $u_e^{\pm} =$

$\sqrt{\frac{1}{2}(1 + \frac{\varepsilon_e^{\pm}}{|E|})}$, $u_h^{\pm} = \sqrt{\frac{1}{2}(1 + \frac{\varepsilon_h^{\pm}}{|E|})}$, $v_e^{\pm} = \alpha_e^{\pm}\sqrt{\frac{1}{2}(1 - \frac{\varepsilon_e^{\pm}}{|E|})}$, $v_h^{\pm} = \alpha_h^{\pm}\sqrt{\frac{1}{2}(1 - \frac{\varepsilon_h^{\pm}}{|E|})}$, with $\alpha_{e(h)}^+ = \alpha_{e(h)}^- = \text{sgn}(\sin\theta_{e(h)})$. Here, $\varepsilon_{e(h)}^+ = \varepsilon_{e(h)}^- = \sqrt{|E|^2 - \Delta_{e(h)}^2}$, with $\Delta_{e(h)} = \Delta_p \sin\theta_{e(h)}$, $\theta_e = \theta_k - \phi$, and $\theta_h = \pi - \theta_k - \phi$ denote the effective pair potentials of electronlike and holelike quasiparticles, respectively [24,31,36], where θ_k depicts the electron incident angle and ϕ represents the angle between the z axis of the p-wave and the normal to the interface (similar to the angle α between the x axis of the d-wave the interface normal in a d-wave superconductor [36]), as shown in Fig. 1(b).

Second, we consider a mixed S-wave pairing and ABM state, whose superconducting order parameter has the following form: $\hat{\Delta}(k) = -\Delta_p \sin\theta_k\sigma_z + \Delta_s i\sigma_y$ [31,37]. Then, the superconducting order parameters split into two independent order parameters $\Delta_{e(h)}^+ = \Delta_p \sin\theta_{e(h)} + \Delta_s$ and $\Delta_{e(h)}^- = \Delta_p \sin\theta_{e(h)} - \Delta_s$, respectively [38]. In this case, the wave function changes to $\psi_1 = [u_e^+, u_e^+, -v_e^+, v_e^+]^T$, $\psi_2 = [u_h^+, u_h^+, -v_h^+, v_h^+]^T$, $\psi_3 = [u_e^-, -u_e^-, v_e^-, v_e^-]^T$, and $\psi_4 = [u_h^-, -u_h^-, v_h^-, v_h^-]^T$. Here, $u_{e(h)}^{\pm}$ and $v_{e(h)}^{\pm}$ have the same form as the former case, with $\varepsilon_{e(h)}^{\pm} = \sqrt{E^2 - (\Delta_{e(h)}^{\pm})^2}$, $\alpha_{e(h)}^{\pm} = \text{sgn}(\Delta_{e(h)}^{\pm})$.

The wave function in the lead region is derived from the Hamiltonian: $\hat{H}_N(k) = \zeta_k - \mu + \vec{M} \cdot \vec{V}$; where ζ_k, and μ denote the kinetic energy and the chemical potential, respectively. The plane wave at the normal metal side can be expressed by a four-component wave function in the Nambu representation:

$$\Psi_N = e^{(ik_Fx)}\begin{pmatrix} e^{ik_Fz} + b_{\uparrow,\uparrow}e^{-ik_Fz} \\ b_{\uparrow,\downarrow}e^{-ik_Fz-\gamma} \\ a_{\uparrow,\uparrow}e^{ik_Fz} \\ a_{\uparrow,\downarrow}e^{ik_Fz+\gamma} \end{pmatrix}. \qquad (4)$$

The first row $e^{ik_Fz} + b_{\uparrow,\uparrow}e^{-ik_Fz}$ of Eqs. (4) describes an electron with a spin-up incident plane wave and a normal reflection wave. The second row $b_{\uparrow,\downarrow}e^{-ik_Fz-\gamma}$ describes an electron with a spin-down wave. The third row $a_{\uparrow,\uparrow}e^{ik_Fz}$ and the fourth row $a_{\uparrow,\downarrow}e^{ik_Fz+\gamma}$ are hole descriptors with a spin-up and a spin-down Andreev reflection wave, respectively. The $\gamma = 0$ in nonmagnetic metal (NM) lead and $\gamma = \infty$ in FM lead [39] describe the evanescent wave. Note that we only consider the incidence of spin-up electrons. Fully polarized ferromagnetic leads contain only spin-up electrons whereas in nonmagnetic leads, the spin-up and spin-down electrons are identical, so it is sufficient to consider spin-up electrons only.

Next, we study the transport properties of the N/S junction. We assume that the N/S interface located at $z = 0$ along the x axis has an infinitely narrow insulating barrier described by the delta function $U = U\delta(z)$ [24,31]. Solving the following boundary conditions [24,31,40]:

$$\Psi_S(0) = \Psi_N(0), \qquad \frac{\partial\Psi_S(z)}{\partial z}\Big|_{z=0} - \frac{\partial\Psi_N(z)}{\partial z}\Big|_{z=0} = U\Psi_S(0), \qquad (5)$$

we obtain $a_{\uparrow,\uparrow(\downarrow)}$ and $b_{\uparrow,\uparrow(\downarrow)}$.

For two-dimensional N/S junctions, the normalized conductance with a bias voltage is [24,40]

$$\sigma(\text{eV}) = \frac{\int_{-\pi/2}^{\pi/2} g^T(\text{eV})\cos\theta \, d\theta}{\int_{-\pi/2}^{\pi/2} g^T(\infty)\cos\theta \, d\theta}, \tag{6}$$

where $g^T(\text{eV}) = \int_0^1 g(|\text{eV} + \frac{1}{\beta} ln\frac{1-f}{f}|)$, and $g(E) = [1 + \frac{1}{2}\sum_{\rho=\uparrow,\downarrow}(|a_{\uparrow,\rho}(\theta,E)|^2 - |b_{\uparrow,\rho}(\theta,E)|^2)]$, $\beta = \frac{1}{k_B T}$. We use the parameter Γ to represents the energy broadening in the calculation [39]. Here, we mainly study the Andreev conductance of the two-dimensional model in the x-z plane, while for the three-dimensional model, the Andreev conductance needs to be integrated in the x-y plane [41].

III. THE CONDUCTANCE AND SURFACE STATE OF ABM STATE

First, we calculated the normalized Andreev conductance between nonmagnetic leads and spin triplet superconducting states at different incident planes, denoted by ϕ. Here, we mainly calculate the Andreev conductance of two common spin-triplet superconductors: the ABM state and the Balian-Werthamer (BW) state [42]. We find that the ABM state can explain the point-contact experiment of Bi/Ni bilayers, but the BW state cannot. For detailed data on the comparison of the two superconducting states, see Appendix A.

In fact, other experimental work has proposed that there may be d-wave superconducting states [43] in Bi/Ni bilayers. The possible existence of a gap-filling mechanism [44] in Bi/Ni bilayer films is also discussed theoretically, which can reasonably explain the experiment. However, in this paper, we mainly study the possible spin-triplet superconducting states in Bi/Ni bilayers based on the point-contact experiments of ferromagnetic leads.

Then, we use the ABM state to fit the experimental results of Bi/Ni bilayer films. Detailed information about the experimental fitting procedure is detailed in Appendix B. Using the parameters obtained from the fitting point-contact experiment, we further calculate the Andreev conductance of ABM-state superconductors. In the subsequent analysis, we mainly set ϕ equal to $0°$ and $60°$. This is because the result of $60°$ is close to the experimental result of the c plane, and the conductance peak is also obvious.

As shown in Figs. 2(a) and 2(b), the conductance near the zero energy changed from a valley to a peak as ϕ increased. As ϕ is zero, the conductivity near the zero energy was valley shaped. Increasing ϕ gradually increases the conductance at zero energy and the conductance peak. Details of the transition of conductance from valley to peak are in Appendix C.

Comparing the density of states localized on the surface (method of calculating LODS is in Appendix D) with the energy band of the ABM state, we observe that the conductivity at zero energy is contributed by the projection of the surface state between the two Weyl points on the incident plane at the zero energy. First, as the local density of states on the surface was consistent with the conductance spectrum, the conductance could be attributed to the strength of the density of states. At $\phi = 0°$ [Fig. 2(c)], the density of states exhibited a funnel-like shape, forming a valley of conductance. As
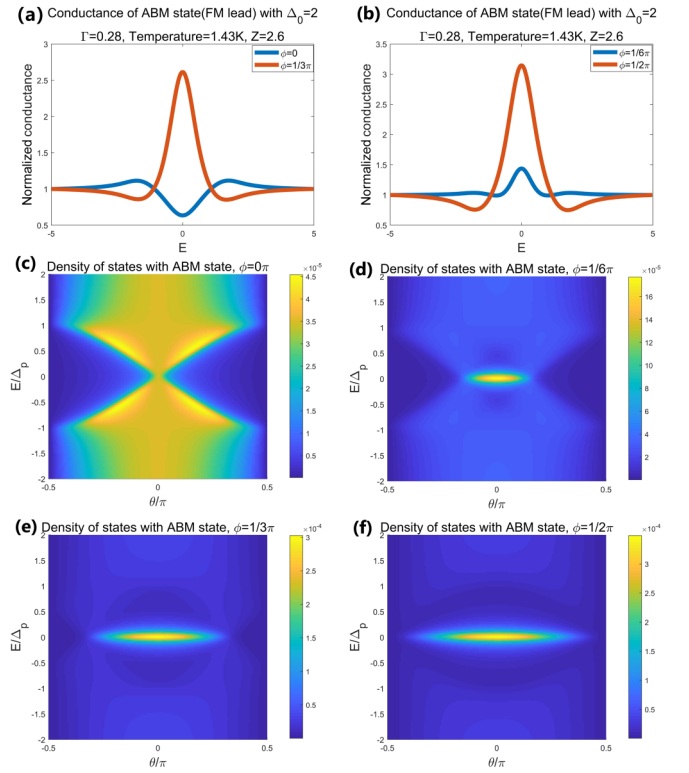

FIG. 2. Conductance and density of states for different incidence planes. Conductance of (a) $\phi = 0°$ and $60°$, (b) $\phi = 30°$ and $90°$; density of states for (c) $\phi = 0°$, (d) $\phi = 30°$, (e) $\phi = 60°$, and (f) $\phi = 90°$. Here, θ is the incident angle, ϕ is represents the angle between the z axis of the p-wave and the normal to the interface. As ϕ increases, the conductance near zero energy increases, and the surface state near the zero energy becomes increasingly obvious. The interfacial parameter was obtained by data fitting to the experimental data of the c face of FM lead.

ϕ increased [Figs. 2(d)–2(f)], the density of states became increasingly concentrated around the zero energy, leading to a more pronounced peak in the conductance spectrum. However, as shown in Fig. 1(b), the band structure of the ABM state was similar to that of Weyl semimetals, with only two Weyl points at zero energy. Previous work reported a Fermi arc between the two Weyl points [45,46]. Comparing the density of states with the band structure, we inferred that the zero-energy state is the projection of the Fermi arc on the incident plane.

Extending to the three-dimensional model, we find that the normalized Andreev conductance is qualitatively consistent with the two-dimensional model. Therefore, our conclusion can be extended to the three-dimensional model. Conductance spectroscopy of the Andreev reflection between ferromagnetic/nonmagnetic leads and the ABM state at different incident planes was consistent with the density of states qualitatively. The interface barrier strength (Z), temperature (T), and impurity multiple scattering (Γ) have influence on the tunneling spectrum. When the interface barrier is stronger, the transparency is lower, and the tunneling spectrum is closer to LDOS. In addition, with the decrease of temperature and multiple scattering, the tunneling spectrum is also closer to LDOS.
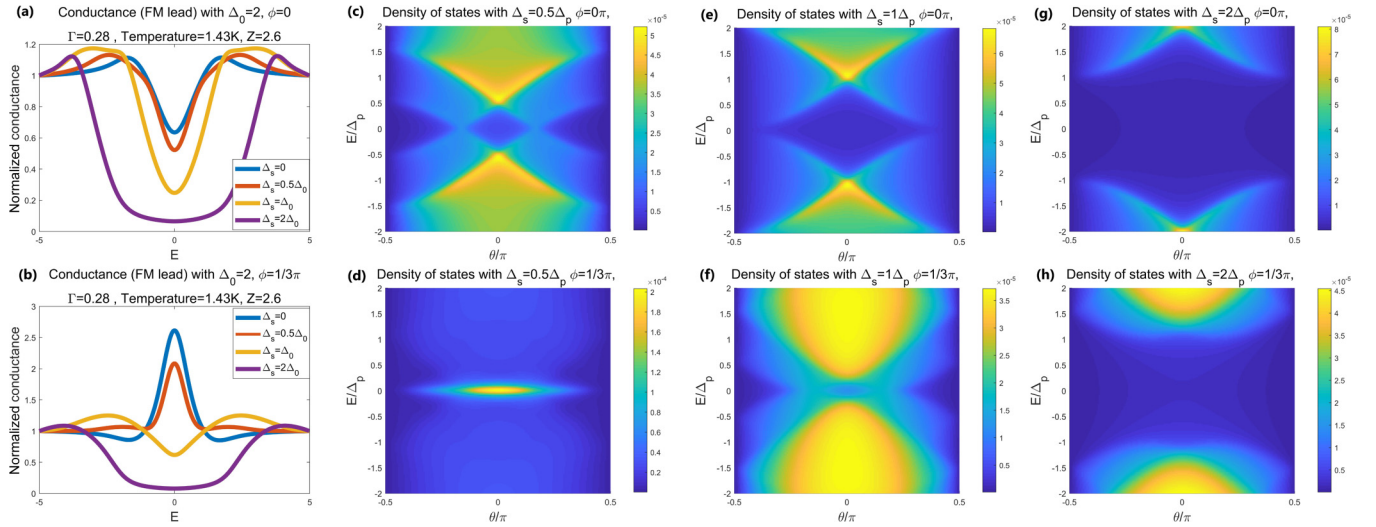
FIG. 3. Conductance with different Δ_s at (a) $\phi = 0°$ and (b) $\phi = 60°$; density of states for different Δ_s and (c) $\Delta_s = 0.5\Delta_p$, (e) $\Delta_s = \Delta_p$, and (g) $\Delta_s = 2\Delta_p$ at $\theta = 0°$, and (d) $\Delta_s = 0.5\Delta_p$, (f) $\Delta_s = \Delta_p$, and (h) $\Delta_s = 2\Delta_p$ at $\theta = 60°$. At ϕ is 0, increasing the S-wave component widened and deepened the valley in the conductance profile by widening the gap in density of states. At $\phi = 60°$ and when the S-wave component is lower than the p-wave component, the surface state and conductance at zero energy gradually disappear with increase of S-wave component. At $\phi = 60°$ and when the S-wave component exceeds the p-wave component and is further increased, a density of states energy gap forms near the zero energy and the conductance valley widens.

IV. MIXTURE OF ABM STATE AND *S*-WAVE STATE

Different pairing states can mix in the Bi/Ni bilayer due to the inversion symmetry breaking [30,31]. Here, we mainly study one of the possible mixed forms: the mixing of p-wave superconducting states and S-wave superconducting states. Next, we studied the Andreev spectroscopy and topological properties of unconventional superconductors composed of the ABM state and S-wave superconductors.

The Andreev conductance was qualitatively consistent with that of the pure ABM state when $\Delta_s < \Delta_p$ [Figs. 3(a) and 3(b)], but with that of the pure S-wave state when $\Delta_s \geqslant \Delta_p$. As the conductance at zero energy is mainly contributed by the zero-energy surface state, we next investigated the effect of the S-wave component on the surface state.

As the S-wave component increased, the surface and bulk states near the zero energy gradually weakened and eventually disappeared [Figs. 3(c)–3(h)]. When $\phi = 0°$, the S-wave component split the funnel-like formation of the previous density of states into two parts: a left and a right part. As the S-wave component increased, the split widened and the two nodes at zero energy gradually moved apart and disappeared, thereby reducing the zero-energy conductance. The splitting increased the density of states in the overlapping parts of the two nodes. Increasing the S-wave component also shifted the higher density region from zero energy, increasing the conductance valley width. However, at $\phi = 60°$, as the S-wave component increased from 0 to the p-wave component, the surface state weakened and disappeared. When the S-wave component exceeded the p-wave component, it split the density of states into two parts. Further increases of the S-wave component gradually increased the distance between the two parts and diminished the conductance at zero energy, widening the conductance valley. Therefore, when the S-wave component is larger than the p-wave component, the

topological surface state disappears. From the perspective of topological phase transition, this is consistent with previous studies [47,48].

Extending to the three-dimensional model, we find that the zero-energy surface state will split gradually with the gradual rotation of the two-dimensional tunnel junction from the x-z plane to the y-z plane. Therefore, the conductance of the three-dimensional model will gradually become a more and more obvious bimodal structure with the increase of the S-wave component, and finally tend to the shape of the pure S-wave case. In addition, when the S-wave component is very small, the zero-energy conductance peak can still appear due to the impurities' multiple scattering and the influence of the temperature.

In summary, the S-wave component reduced the surface state and the conductance at zero energy. Using the two-dimensional tunnel junction model, we found that when the S-wave component was less than the p-wave component, the conductance profile resembled that of the pure ABM state. Using the three-dimensional model, we find that when the S-wave component is very small, the normalized conductance of the mixing superconducting state and the pure ABM state is qualitatively consistent and can also match the point-contact experiment [24]. The energy band retained it's zero-energy nodes in this case. However, when the S-wave component exceeded the p-wave component, the conductance profile formed a shape of the valley and the energy band formed a globe gap. Therefore, when the S-wave component was small, the conductance was qualitatively consistent with the point-contact results [24] but the energy band failed to explain the time-domain THz spectroscopy [29]. In contrast, when the S-wave component was large, the energy band was consistent with the time-domain THz spectroscopy [29] but the conductance failed to explain the point-contact results [24].
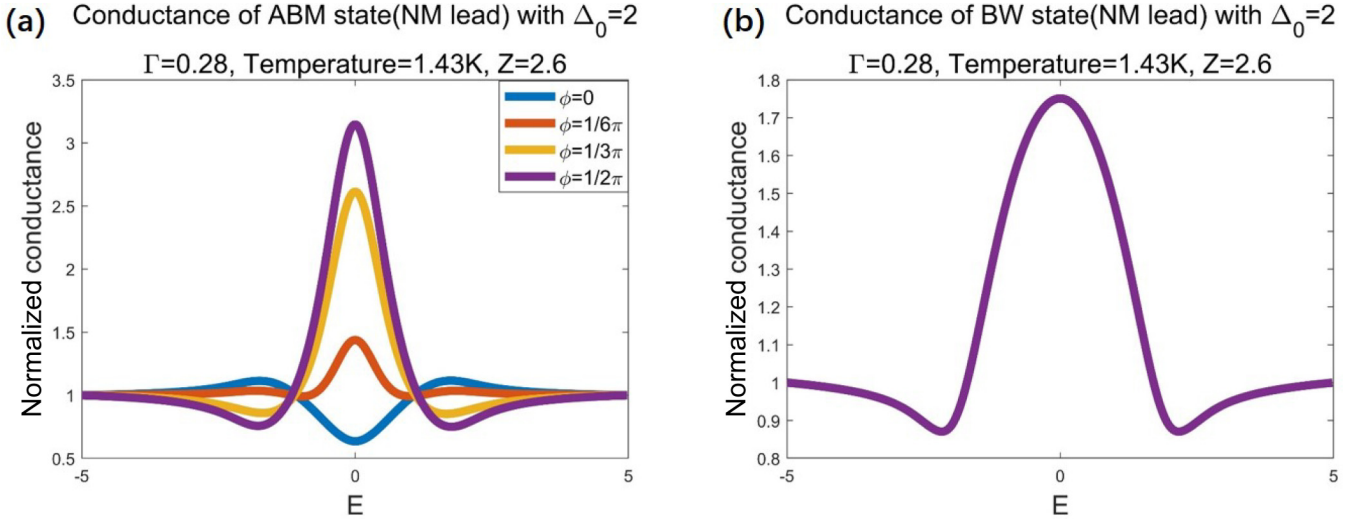
FIG. 4. Comparison of the Andreev conductance between ABM state (a) and BW state (b). At different incident planes, the Andreev conductance of ABM state shows the structure of peak and valley, respectively. Therefore, the ABM state can be used to explain the point-contact experimental results of Bi/Ni bilayers. However, the conductance of BW state always shows a peak structure at different incident planes, so it cannot explain the point-contact experimental results of Bi/Ni bilayers.

V. SUMMARY

We studied the Andreev reflection conductance between ferromagnetic lead and two types of superconductors (a pure ABM state superconductor and a mixed state ABM state and S-wave state) by the BTK method. First, we found that the conductance of the pure ABM state is consistent with that of point-contact experiments [24]. Second, the result of the mixed state with a small S-wave component was qualitatively consistent with that of the pure ABM state and the point-contact experiments [24]. However, when the S-wave component was large, the conductance deviated from the point results [24] because the gap opened and widened in the energy band. We also calculated the local density of states and attributed the conductance peak at zero energy to the surface state of the ABM-state component. Our work provides some complementary explanations for the results of recent experiments.

APPENDIX A: COMPARISON OF THE ANDREEV CONDUCTANCE BETWEEN ABM STATE AND BW STATE

The common spin-triplet superconducting states include the ABM state and BW state. To better understand the results of the point-contact experiment, we compare the Andreev conductance of the two superconducting states at different incident planes.

As shown in Fig. 4, when the incident plane is different, the Andreev conductance of ABM state superconductors appears in the form of peak and valley respectively, which is similar to the point contact experimental results of Bi/Ni bilayer films. Therefore, the ABM state can be used to explain the point contact experiment of Bi/Ni bilayer films. However, due to the isotropic pairing potential in the BW state, the normalized conductance does not change when the incident surface is different. Therefore, the BW state can not be used to explain the point contact experimental results of Bi/Ni bilayers.

Comparing the Andreev conductance of the two spin triplet superconducting states, we think that there may be ABM state components in the Bi/Ni bilayers.

APPENDIX B: FITTING OF THE EXPERIMENTAL RESULTS

Using our model developed in Section II we fited the experimentally obtained normalized Andreev reflection conductances in FM and NM lead (see Fig. 5). The fittings were obtained different incident surfaces with different interface parameters and different (ϕ).

For the results of the NM lead, the parameters were set as follows: $\Delta_0 = 2.2, Z = 2.2, \Gamma = 0.2, T = 1.43$ K, $\phi = 0.25\pi$ in the a plane; $\Delta_0 = 2.2, Z = 0.64, \Gamma = 0.33, T = 1.43$ K, $\phi = 0.0\pi$ in the b plane; and $\Delta_0 = 2.2, Z = 1.8, \Gamma = 0.2, T = 1.43$ K, $\phi = 0.3\pi$ in the c plane. For the results of the FM lead, the parameters were set to $\Delta_0 = 2.0, Z = 1.8, \Gamma = 0.0.05, T = 1.43$ K, $\phi = 0.3\pi$ in the a plane, $\Delta_0 = 2.0, Z = 0.698, \Gamma = 0.6, T = 1.43$ K, $\phi = 0.0\pi$ in the b plane, and $\Delta_0 = 2.0, Z = 2.6, \Gamma = 0.28, T = 1.43$ K, $\phi = 0.21\pi$ in the c plane.
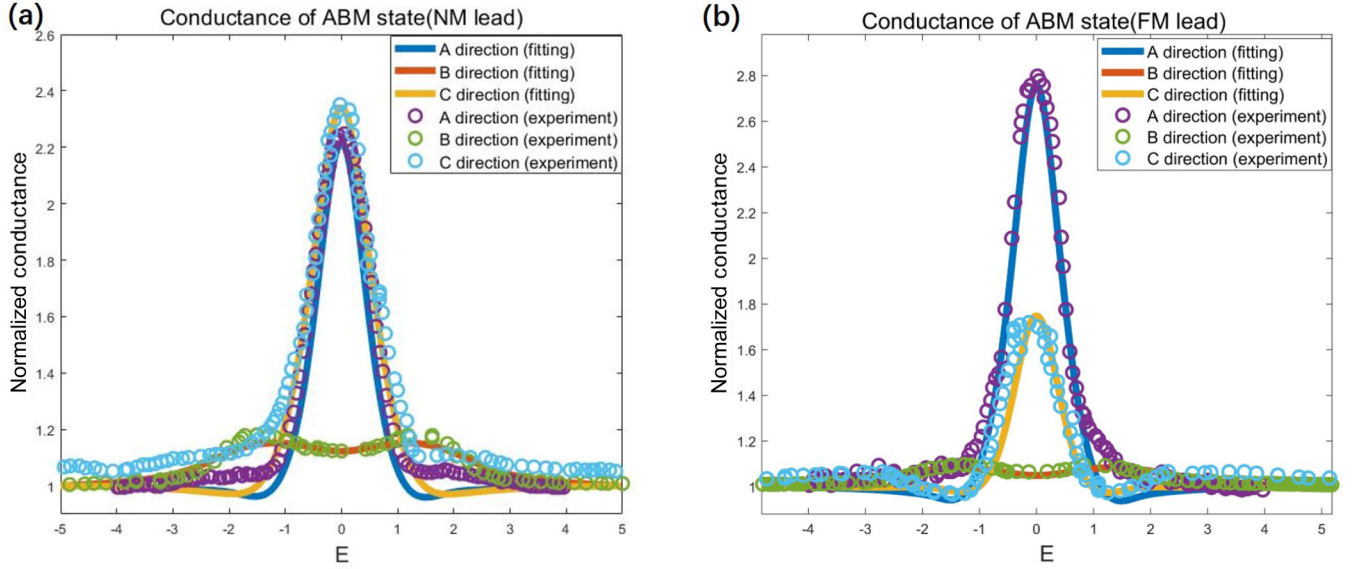
FIG. 5. Fitting of the experimental conductance-energy profiles in different types of lead: FM(right) and NM(left). Here, the order parameter in the pure ABM state is calculated by Eq (2).

APPENDIX C: THE CONDUCTANCE WITH DIFFERENT INCIDENCE PLANE

To further study the transition of conductance from valley to peak, we calculate the Andreev conductance when ϕ increases gradually from $0°$. The results are plotted in Fig. 6. We find that with the slow increase of ϕ, the conductance changes slowly from valley to peak shape.

APPENDIX D: SURFACE GREEN'S FUNCTION

Here, we briefly introduce the method of calculating the surface Green's function [49]. First, we discretize the Hamiltonian along the z direction and label each layer with its cor-
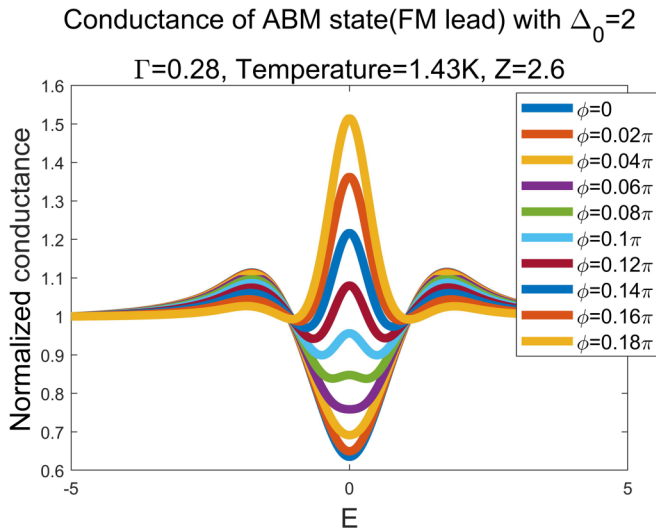
responding z value (layer $i = 1 - n$). Then, the Hamiltonian is given by

$$
H = \begin{pmatrix} H_{0l,0l} & H_{0l,1l} & & & \\ H_{1l,0l} & H_{0l,0l} & & & \\ & & \ddots & \ddots & \\ & & \ddots & H_{0l,0l} & H_{0l,1l} \\ & & & H_{1l,0l} & H_{0l,0l} \end{pmatrix}, \quad \text{(D1)}
$$

where $H_{il,i'l}$ denotes the coupling between the i and i' layers. After discretizing the Hamiltonian, the surface Green's function is obtained by the following procedure: First, define the parameters:

$$
\alpha_0 = (\omega - H_{0l,0l})^{-1} H_{1l,0l}, \quad \beta_0 = (\omega - H_{0l,0l})^{-1} H_{0l,1l}. \quad \text{(D2)}
$$

Second, iterate the expressions until $\alpha_i \to 0$, $\beta_i \to 0$:

$$
\alpha_i = (1 - \alpha_{i-1}\beta_{i-1} - \beta_{i-1}\alpha_{i-1})^{-1} \alpha_{i-1}^2,
$$
$$
\beta_i = (1 - \alpha_{i-1}\beta_{i-1} - \beta_{i-1}\alpha_{i-1})^{-1} \beta_{i-1}^2. \quad \text{(D3)}
$$

Third, define $T = \alpha_0 + \beta_0\alpha_1 + \cdots + \beta_0\beta_1 \cdots \beta_{n-1}\alpha_n$. The surface Green's function is : $g_{00} = \{\omega - H_{0l,0l} - H_{0l,1l}T\}^{-1}$. From this function, we obtain the density of states on the superconductor surface.

FIG. 6. The variation of conductance with the incident plane. With the change of ϕ, the conductance gradually changes from valley to peak.

APPENDIX E: INFLUENCE OF *S*-WAVE COMPONENTS ON ENERGY BAND, CONDUCTANCE, AND SURFACE STATES

We first calculated the density of states for different *S*-wave components and incident planes. The *S*-wave exerted a huge influence on the energy band and density of states, splitting both the original energy band [Figs. 7(a)–7(d)] and the original hourglass profile [Figs. 7(e)–7(g)] into two parts.

As shown in Figs. 7(i)–7(k), 7(m)–7(o), and 7(q)–7(s), the *S*-wave component also decreased the surface density of states. At $\Delta_s = \Delta_p$, the surface states disappeared completely.
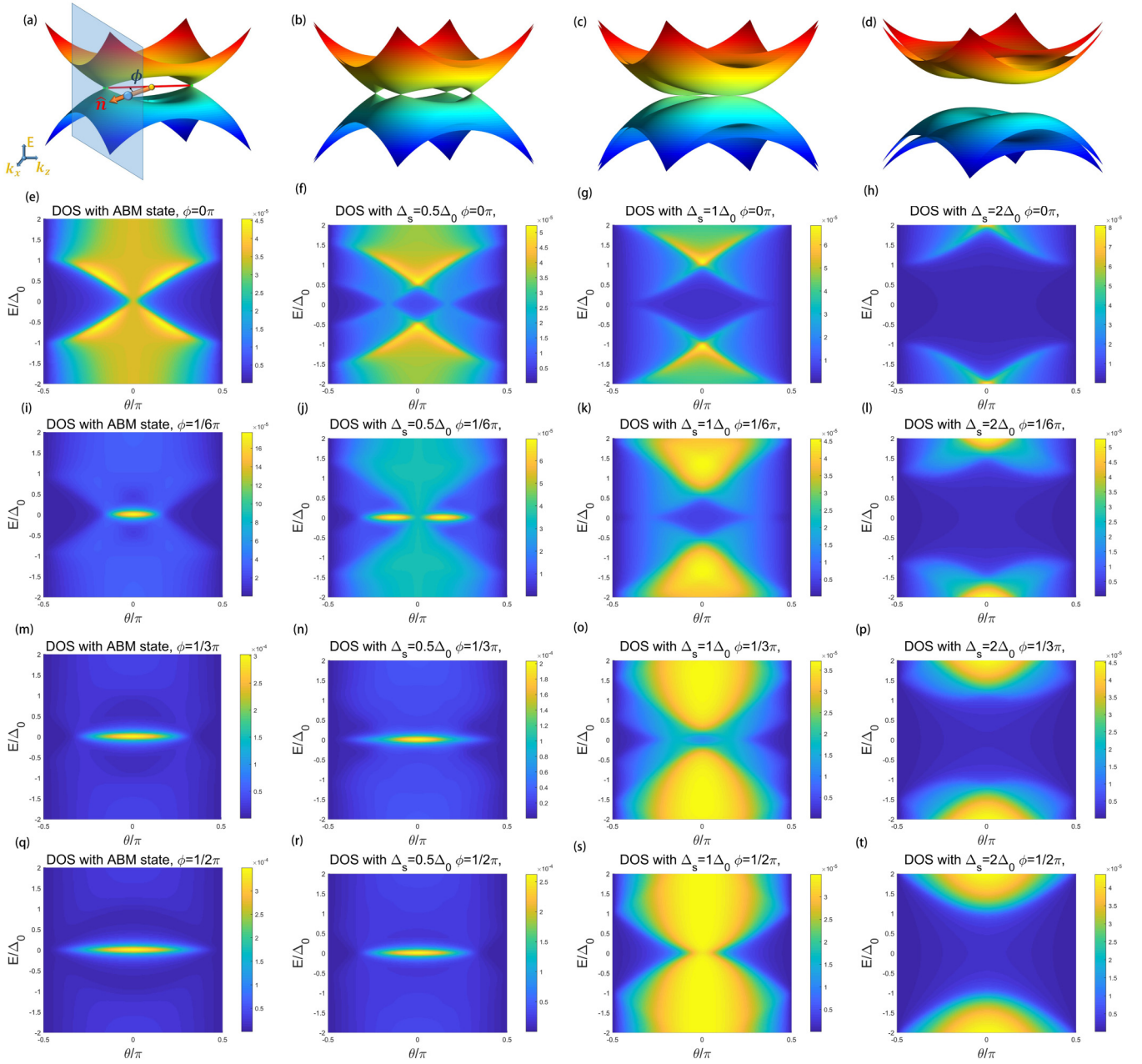
FIG. 7. Influence of Δ_s on the band structure and local density of states for different incident faces between the FM lead and superconductor. (a)–(d) show the energy band in pure ABM states, $\Delta_s = 0.5\Delta_p$, $\Delta_s = \Delta_p$, and $\Delta_s = 2\Delta_p$, respectively; (e)–(h), (i)–(l), (m)–(p), and (q)–(t) show the local density of states when $\phi = 0°$, $\phi = 30°$, $\phi = 60°$, and $\phi = 90°$ in those superconductivity states. The Δ_s decreases the conductance near zero energy and suppresses the surface state. When $\Delta_s \geqslant \Delta_p$ and $\phi > 0$, the surface state and conductance peak vanished.

Moreover, the S-wave component created a growing gap in both the energy band and density of states for different incident planes [Figs. 7(c) and 7(d), 7(k) and 7(l), 7(o) and 7(p), 7(s) and 7(t)].

Second, we calculated the influence of the S-wave component on the conductance for different incident planes between the FM lead and superconductor. As shown in Figs. 8(e)–8(h), the S-wave component decreased the conductance near zero energy. When $\Delta_s < \Delta_p$, the conductance profile resembled

that of Andreev conductance in the pure ABM state; when $\Delta_s \geqslant \Delta_p$, it was similar to the Andreev conductance in a pure S-wave superconductor.

The influence of the S-wave component on the conductance spectrum for different incident planes is shown in Figs. 8(e)–8(x). The conductance spectrum resembled that of the local density of states. When $\Delta_s < \Delta_p$ and ϕ was nonzero, the S-wave component decreased the conductance near the zero energy by decreasing the surface density of states near zero
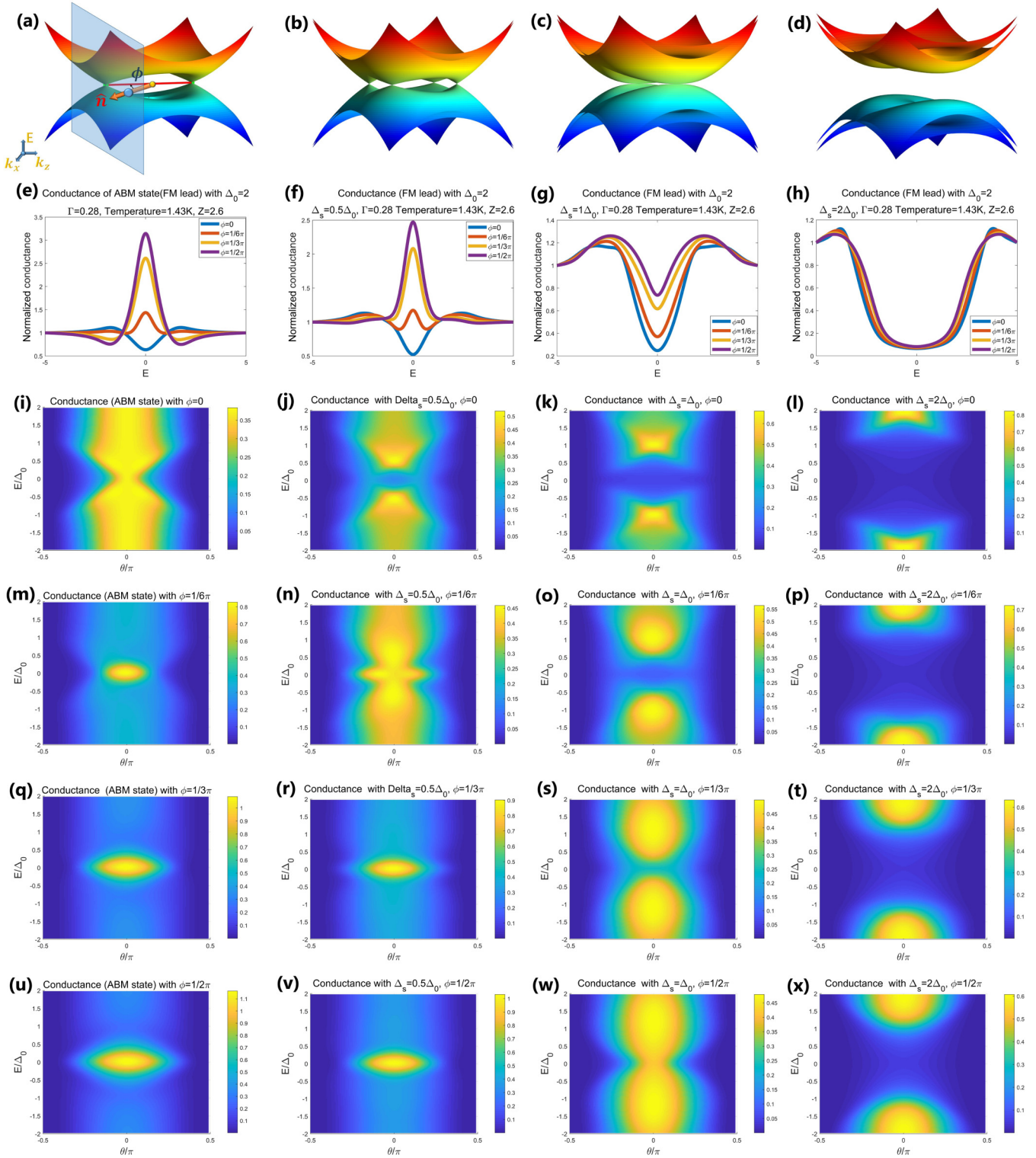
FIG. 8. Influence of Δ_s on the conductance and its spectrum for different incident planes between the FM lead and superconductor. (a)–(d) show the schematic diagram of energy band in pure ABM states, $\Delta_s = 0.5\Delta_p$, $\Delta_s = \Delta_p$, and $\Delta_s = 2\Delta_p$, respectively; (e)–(h) show the conductance in those superconductivity states; (i)–(l), (m)–(p), (q)–(t), and (u)–(x) show the conductance spectrum when $\phi = 0°$, $\phi = 30°$, $\phi = 60°$, and $\phi = 90°$ in those superconductivity states. The Δ_s decreases the conductance near the zero-energy region. When $\Delta_s \geqslant \Delta_p$, the conductance peak vanishes.

energy. However, when $\Delta_s < \Delta_p$ and $\phi = 0$, it decreased the conductance near zero energy by splitting the density of states. Finally, when $\Delta_s \geqslant \Delta_p$, it decreased the conductance far from zero energy by expanding the gap between the high density of states regions.

Next, we calculated the influence of the S-wave component on the conductance for different incident planes between NM leads and superconductors. The conductance and its spectrum were different in magnitude but qualitatively consistent with those of FM leads in the same situations.

[1] M. Tinkham, *Introduction to Superconductivity*, 2nd ed., Dover Books on Physics (Courier Corporation, Dover, 2004).

[2] D. Vollhardt, P. Wolfle, and R. B. Hallock, Phys. Today **44**(8), 60 (1991).

[3] T. Mizushima, Y. Tsutsumi, T. Kawakami, M. Sato, M. Ichioka, and K. Machida, J. Phys. Soc. Jpn. **85**, 022001 (2016).

[4] F. Romeo and R. Citro, Phys. Rev. Lett. **111**, 226801 (2013).

[5] C. Nayak, S. H. Simon, A. Stern, M. Freedman, and S. Das Sarma, Rev. Mod. Phys. **80**, 1083 (2008).

[6] M. Z. Hasan and C. L. Kane, Rev. Mod. Phys. **82**, 3045 (2010).

[7] X.-L. Qi, T. L. Hughes, S. Raghu, and S.-C. Zhang, Phys. Rev. Lett. **102**, 187001 (2009).

[8] S. Ryu, A. P. Schnyder, A. Furusaki, and A. W. W. Ludwig, New J. Phys. **12**, 065010 (2010).

[9] N. Read and D. Green, Phys. Rev. B **61**, 10267 (2000).

[10] D. A. Ivanov, Phys. Rev. Lett. **86**, 268 (2001).

[11] G. E. Volovik, JETP Lett. **90**, 587 (2009).

[12] G. E. Volovik, JETP Lett. **90**, 398 (2009).

[13] R. Roy, Phys. Rev. Lett. **105**, 186401 (2010).

[14] S. Das Sarma, C. Nayak, and S. Tewari, Phys. Rev. B **73**, 220502(R) (2006).

[15] S. Murakawa, Y. Tamura, Y. Wada, M. Wasai, M. Saitoh, Y. Aoki, R. Nomura, Y. Okuda, Y. Nagato, M. Yamamoto, S. Higashitani, and K. Nagai, Phys. Rev. Lett. **103**, 155301 (2009).

[16] S. Kashiwaya, H. Kashiwaya, H. Kambara, T. Furuta, H. Yaguchi, Y. Tanaka, and Y. Maeno, Phys. Rev. Lett. **107**, 077003 (2011).

[17] S. Kashiwaya, H. Kashiwaya, K. Saitoh, Y. Mawatari, and Y. Tanaka, Physica E: Low-dimensional Syst. Nanostruct. **55**, 25 (2014), topological Objects.

[18] D. J. Thouless, M. Kohmoto, M. P. Nightingale, and M. den Nijs, Phys. Rev. Lett. **49**, 405 (1982).

[19] B. I. Halperin, Phys. Rev. B **25**, 2185 (1982).

[20] Y. Tanaka, M. Sato, and N. Nagaosa, J. Phys. Soc. Jpn. **81**, 011013 (2011).

[21] S. Kashiwaya, Y. Tanaka, M. Koyanagi, H. Takashima, and K. Kajimura, Phys. Rev. B **51**, 1350 (1995).

[22] S. Kashiwaya and Y. Tanaka, Rep. Prog. Phys. **63**, 1641 (2000).

[23] X.-X. Gong, H.-X. Zhou, P.-C. Xu, D. Yue, K. Zhu, X.-F. Jin, H. Tian, G.-J. Zhao, and T.-Y. Chen, Chin. Phys. Lett. **32**, 067402 (2015).

[24] G. Zhao, X. Gong, J. He, J. Gifford, H. Zhou, Y. Chen, X. Jin, C. Chien, and T. Chen, arXiv:1810.10403 (2018).

[25] S.-P. Chao, Phys. Rev. B **99**, 064504 (2019).

[26] P. W. Anderson and P. Morel, Phys. Rev. Lett. **5**, 136 (1960).

[27] P. W. Anderson and W. F. Brinkman, Phys. Rev. Lett. **30**, 1108 (1973).

[28] A. P. Schnyder and P. M. Brydon, J. Phys.: Condens. Matter **27**, 243201 (2015).

[29] P. Chauhan, F. Mahmood, D. Yue, P.-C. Xu, X. Jin, and N. P. Armitage, Phys. Rev. Lett. **122**, 017002 (2019).

[30] M. Sato and Y. Ando, Rep. Prog. Phys. **80**, 076501 (2017).

[31] E. Bauer and M. Sigrist, *Non-Centrosymmetric Superconductors: Introduction and Overview* (Springer Science & Business Media, Berlin, 2012), Vol. 847.

[32] G. E. Blonder, M. Tinkham, and T. M. Klapwijk, Phys. Rev. B **25**, 4515 (1982).

[33] Y. Peng, Y. Bao, and F. von Oppen, Phys. Rev. B **95**, 235143 (2017).

[34] A. Umerski, Phys. Rev. B **55**, 5266 (1997).

[35] M. P. L. Sancho, J. M. L. Sancho, J. M. L. Sancho, and J. Rubio, J. Phys. F: Metal Physics **15**, 851 (1985).

[36] Y. Tanaka and S. Kashiwaya, Phys. Rev. Lett. **74**, 3451 (1995).

[37] P. A. Frigeri, D. F. Agterberg, A. Koga, and M. Sigrist, Phys. Rev. Lett. **92**, 097001 (2004).

[38] C. Iniotakis, N. Hayashi, Y. Sawa, T. Yokoyama, U. May, Y. Tanaka, and M. Sigrist, Phys. Rev. B **76**, 012501 (2007).

[39] T. Y. Chen, Z. Tesanovic, and C. L. Chien, Phys. Rev. Lett. **109**, 146602 (2012).

[40] T. Yokoyama, Y. Tanaka, and J. Inoue, Phys. Rev. B **72**, 220504(R) (2005).

[41] M. Yamashiro, Y. Tanaka, Y. Tanuma, and S. Kashiwaya, J. Phys. Soc. Jpn. **67**, 3224 (1998).

[42] R. Balian and N. Werthamer, Phys. Rev. **131**, 1553 (1963).

[43] X. Gong, M. Kargarian, A. Stern, D. Yue, H. Zhou, X. Jin, V. M. Galitski, V. M. Yakovenko, and J. Xia, Sci. Adv. **3**, e1602579 (2017).

[44] R. Ghadimi, M. Kargarian, and S. A. Jafari, Phys. Rev. B **100**, 024502 (2019).

[45] X. Su-Yang, B. Ilya, A. Nasser, N. Madhab, B. Guang, Z. Chenglong, S. Raman, C. Guoqing, Y. Zhujun, and L. Chi-Cheng, Science **349**, 613 (2015).

[46] S. Jia, S. Y. Xu, and M. Z. Hasan, Nat. Mater. **15**, 1140 (2016).

[47] Y. Tanaka, T. Yokoyama, A. V. Balatsky, and N. Nagaosa, Phys. Rev. B **79**, 060505(R) (2009).

[48] P. Burset, F. Keidel, Y. Tanaka, N. Nagaosa, and B. Trauzettel, Phys. Rev. B **90**, 085438 (2014).

[49] M. P. L. Sancho, J. M. L. Sancho, and J. Rubio, J. Phys. F: Metal Phys. **14**, 1205 (1984).